Journal of Geophysical Research: Oceans

RESEARCH ARTICLE
10.1029/2018JC014093

Variability of Suspended Particle Properties Using Optical Measurements Within the Columbia River Estuary

Jing Tao[1], **Paul S. Hill**[1], **Emmanuel S. Boss**[2], **and Timothy G. Milligan**[3]

[1]Department of Oceanography, Dalhousie University, Halifax, Nova Scotia, Canada, [2]School of Marine Science, University of Maine, Orono, ME, USA, [3]Fisheries and Oceans Canada, Bedford Institute of Oceanography, Dartmouth, Nova Scotia, Canada

Key Points:
- Optical properties provide a good representation of particle dynamics in the Columbia River Estuary
- Variations of alternative optical proxies for particle size are different to the expected trend at salinity transition zone
- Observations are consistent with a model of preferential flocculation of medium-sized particles

Correspondence to:
J. Tao,
jing.tao@dal.ca

Citation:
Tao, J., Hill, P. S., Boss, E. S., & Milligan, T. G. (2018). Variability of suspended particle properties using optical measurements within the Columbia River Estuary. *Journal of Geophysical Research: Oceans*, *123*. https://doi.org/10.1029/2018JC014093

Received 18 APR 2018
Accepted 9 AUG 2018
Accepted article online 22 AUG 2018

Abstract Optical properties are used to understand the spatial and temporal variability of particle properties and distribution within the Columbia River Estuary, especially in the salinity transition zone and in the estuarine turbidity maximum region. Observations of optical properties in the Columbia River Estuary are consistent with the established model that the river water brings more organic, smaller particles into the estuary, where they flocculate and settle into the salt wedge seaward of the density front. Large tidal currents resuspend mineral-rich, larger aggregates from the seabed, which accumulate at the density front. Optical proxies for particle size (beam attenuation exponent γ and backscattering exponent γ_{bb}) are compared to conventional measurements. The γ and γ_{bb} are different to the expected trend with Sauter mean diameter D_s of suspended particles from low- to medium-salinity waters (LMW). D_s increases in the LMW as does the γ derived from a WET Labs ac-9, which indicates that the particle population dominating the ac-9 is decreasing in size. The most likely explanation is that flocculation acting at LMW transfers mass preferentially from medium-sized particles to large-sized particles that are out of the size range to which the ac-9 is most sensitive; γ_{bb} shows no trend in the LMW. Since γ_{bb} is a proxy of proportion of fine particles versus large flocs, the variation of γ_{bb} may be insensitive to changes in the medium-sized particles. The overall results demonstrate that γ_{bb} is a reliable proxy for changes in particle size in a stratified environment.

Plain Language Summary Suspended particles delivered by rivers affect water quality in estuaries, so effective and economical monitoring of the variability of particles is particularly important in environmental management. Direct measurements of suspended particle size, concentration, and composition from water samples require substantial time and labor, which has driven efforts to develop indirect, yet accurate, alternative measurements of particle properties. In this study, we used optical instruments to measure particle variability within the Columbia River Estuary. The observations demonstrate that the river water delivered smaller, organic particles to the estuary, where they aggregated with one another and deposited to the seafloor. Large tidal currents resuspended mineral-rich, larger aggregates from the seafloor, and these aggregates accumulated in the region where river waters encountered coastal ocean waters that flowed into the estuary. We observed that optical measurements related to particle size were different from the expected trend in the transition zone between fresh, river water and salty, coastal water. This unexpected trend requires more study, but we propose that it was caused by preferential aggregation of medium-sized organic-rich particles into large particles. This process would affect the processing of carbon, nutrients, and contaminants in estuaries.

1. Introduction

Estuaries are semienclosed coastal bodies of water in which sea water from the ocean mixes with fresh water delivered by drainage of the land (Pritchard, 1967). Mixing causes extensive biogeochemical transformation of the dissolved and particulate constituents delivered by fresh water discharge, so estuaries act as filters that selectively remove some fresh water constituents while allowing others to flow into the coastal ocean (e.g., Crump et al., 2017). These transformations affect the cycling of carbon and nutrients in estuarine and coastal waters, and they influence the distribution and fate of contaminants (McGuirk Flynn, 2008; Small & Prahl, 2004; Wolanski, 2007).

Much of the organic carbon and nutrients are in particulate form, and many contaminants adsorb readily to particle surfaces. The importance of particles in estuaries has motivated extensive research into their

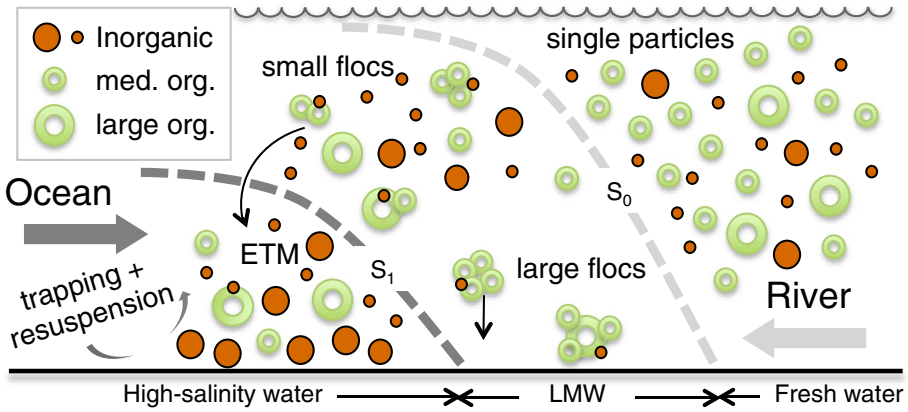

Figure 1. Schematic diagram of particle dynamics in an estuary. The wave line denotes the air-water interface. The dashed curves S_0 and S_1 separate three zones: fresh water, low- to medium-salinity water (LMW) and high-salinity water. Riverine organic and inorganic particles are delivered to an estuary as single particles. In the LMW, flocculation transfers mass into larger flocs. Some of the newly formed larger flocs deposit in the vicinity of the salinity intrusion into the estuary. Smaller flocs are transported seaward, grow larger by flocculating with locally produced and other riverine particles, sink to the bottom layer, and are advected landward by the residual flow. Mineral particles and larger aggregates are resuspended and trapped in an estuarine turbidity maximum (ETM). Modified from Wolanski (2007).

transport, trapping, and transformation and that research has produced a generalized model (Figure 1) for estuarine particle dynamics (e.g., Wolanski, 2007). Riverine organic and inorganic particles are delivered to an estuary as single particles. As mixing with sea water causes salinity to increase to a few parts per thousand, particles that collide with one another stick, either because of electrochemical coagulation or because of flocculation caused by bonding of particles by organic molecules (Hill et al., 2007). The resulting large, loosely bound, and fragile agglomerations of particles typically are called *flocs*. The formation of flocs is important because they sink much faster than their constituent particles (Hill et al., 2000; Milligan et al., 2007). The larger settling velocities cause larger, faster-sinking flocs to deposit, often temporarily, to the seabed in the vicinity of head of the dense intrusion of saltier water into the estuary. Flocs form in low turbulence and break up under high shear stress (Kranck & Milligan, 1992; Milligan et al., 2001), so they have a dynamic size distribution. Smaller flocs are transported seaward in the fresher water that flows over the salinity intrusion. In the fresher surface waters, small flocs interact with locally produced organic matter to form larger flocs that also sink to the bottom. These flocs are transported back into the estuary by near-bed residual flow caused by entrainment of seawater into the seaward flowing fresh water at the surface. The seaward transport of some sea water at the surface is compensated by landward transport of sea water near the seabed. The combination of initial deposition of large flocs at the head of the salinity intrusion and the landward transport of flocs removed from the surface layer further down estuary leads to accumulation of sediment in an estuarine turbidity maximum (ETM). Flocs that are retained and continually cycled between the bed and the suspension eventually become compacted, and the bonds between component particles become stronger. These tougher agglomerations of particles are referred to as *aggregates* (Milligan et al., 2001). The settling velocity of aggregates is higher than the flocs (Milligan et al., 2001).

This conceptual model of particle transport in estuaries was built in large part from in situ observations of particle size gathered with underwater cameras (e.g., Eisma et al., 1983, 1991, 1996; Kranck & Milligan, 1992; Wolanski & Gibbs, 1995) and instruments that measure the near-forward angular distribution of scattered light (e.g., Sequoia Scientific LISST 100; Braithwaite et al., 2010; Gartner et al., 2001; Guo et al., 2017; Sahin et al., 2017). These same instruments, however, have limited potential to develop more complete understanding of the complexity of particle transport and transformation in estuaries. In particular, because the position of the salinity intrusion varies widely in response to changes in tidal stage, tidal range, and river flow (MacCready, 1999), rapid changes in particle concentration, size, and composition occur in space and in time in estuaries. Conventional particle sizing instruments are large and relatively expensive, so it is not practical to deploy multiple instruments to resolve spatial and temporal variability. Furthermore, because light is scattered by small-scale differences in fluid density, instruments that use the near-forward distribution of scattered light to infer size are prone to error in stratified parts of estuaries (Mikkelsen et al., 2008; Tao et al., 2017).

The goal of this research is to evaluate the utility of a set of optical proxies (OPs) for particle properties (PPs) in resolving particle dynamics in stratified estuaries, especially for particle size variability. The exponents of the particulate beam attenuation spectrum and of the particulate optical backscatter spectrum, which have been linked to the particle size distribution (PSD; Boss, Pegau, et al., 2001; Boss, Twardowski, et al., 2001; Morel, 1973; Slade & Boss, 2015), were estimated with two sets of measurements in the Columbia River Estuary (CRE). The first set was gathered on an along-river transect that spanned the critical transition from fresh to medium salinity waters. The second set was gathered at an anchor station located in a part of the CRE through which the ETM migrated on an ebb tide. The spatial and temporal variability in the exponents were compared to conventional measurements of particle size. Optical proxies for particle concentration and composition also were measured and used to assist in the interpretation of observed patterns of variability in the exponents.

1.1. Links Between Particle, Optical, and Microphysical Properties

Because substantial time and labor are required to measure PPs directly, in situ optical instruments have been developed to provide simple, automated, and nearly continuous measurements of PPs over a range of forcing conditions. These in situ optical measurements also avoid issues of handing of water samples, which can alter the particulate size distribution (Reynolds et al., 2010). The PPs have been retrieved from the inherent optical properties of particles, such as particulate attenuation coefficient ($c_p(\lambda)$, m^{-1}), absorption coefficient ($a_p(\lambda)$, m^{-1}), scattering coefficient ($b_p(\lambda)$, m^{-1}), backscattering coefficient ($b_{bp}(\lambda)$, m^{-1}), and near-forward scattering (Boss, Taylor, et al., 2009; Effler et al., 2013; Neukermans et al., 2012). Those inherent optical properties have been used to study PSD (Agrawal & Traykovski, 2001; Bale & Morris, 1987; Boss, Pegau, et al., 2001, Boss, Twardowski et al., 2001; Ellis et al., 2004; Hill et al., 2011), suspended particle concentration (Boss, Slade, & Hill, 2009; Jones & Wills, 1956; Neukermans et al., 2012; Spinrad et al., 1983) and particle composition (Babin et al., 2003; Peng & Effler, 2007; Twardowski et al., 2001; Woźniak et al., 2010).

PSD in marine waters is a fundamental property of particle assemblages that is influenced by biological growth, flocculation, deflocculation, resuspension, and deposition (Xi et al., 2014). The PSD also affects particulate light scattering and vertical sediment flux. PSDs are sometimes approximated by a power law (Junge-like) distribution.

$$N(D) = N(D_0)(D/D_0)^{-\xi}, \tag{1}$$

where $N(D)$ is the number of particles per unit volume per unit bin width (in $L^{-1}\cdot\mu m^{-1}$ or m^{-4}). D_0 is a reference diameter (in μm). The exponent of the PSD, ξ, is the PSD power law exponent with typical values between 2.5 and 5, and 4 being a common oceanic value (Boss, Pegau, et al., 2001; Boss et al., 2013; Stramski & Kiefer, 1991; Slade & Boss, 2015). Assuming that the PSD is described well by the power law distribution, the PSD exponent is theoretically related to the spectral exponent of particulate beam attenuation and particulate backscattering (Boss, Pegau, et al., 2001; Boss, Twardowski et al., 2001; Hulst & van de Hulst, 1957; Morel, 1973; Stramska et al., 2003; Volz, 1954). The beam attenuation exponent, γ, is computed from $c_p(\lambda)$ spectra by fitting it with the following power law relationship with wavelength

$$c_p(\lambda) = c_p(\lambda_0)(\lambda/\lambda_0)^{-\gamma}, \tag{2}$$

where λ_0 is a reference wavelength (in nm). In highly energetic coastal environments, the power law formulation with a single exponent provides a poor description of the PSD (Reynolds et al., 2010). The exponent of the number PSD is insensitive to the changes in larger particles, so it is better to quantify the PSD changes by other parameters such as average particle size and Satuer mean diameter. Slade and Boss (2015) showed that the spectral exponent of c_p is a proxy for average suspended particle size (D_{avg}), with γ inversely and linearly related to D_{avg} derived from LISST-100X (Laser In-Situ Scattering and Transmissometry) PSD data for measurements performed in a bottom boundary layer.

The backscattering exponent γ_{bb}, which is computed from $b_{bp}(\lambda)$ spectra using an equation equivalent to equation (2), was also found to be an indicator of particle size in a similar manner to γ. Based on Slade and Boss (2015) observations, γ and γ_{bb} can be used to infer changes in particle size, at least for nonalgal particle-dominated waters such as river plumes and bottom boundary layers. The spectral exponent of c_p and b_{bp} have been estimated in the various waters, and the range of reported values of γ is from 0.016 to 1.5 (D'Sa et al., 2007; Huang et al., 2016; Reynolds et al., 2016).

Numerous studies have used optical backscattering sensors to assess suspended particulate matter (SPM) concentration (e.g., Creed et al., 2001; Downing, 2006; Jouon et al., 2008; McKee & Cunningham, 2006; Snyder

et al., 2008). The particulate backscattering coefficient b_{bp} is linearly proportional to the SPM concentration in open ocean and coastal waters, allowing it to be used as a proxy for particulate mass (Boss, Taylor, et al., 2009; Neukermans et al., 2012; Tao et al., 2017).

Particulate matter contains both organic and inorganic particles, whose relative concentrations vary in coastal waters. The bulk index of refraction is a useful parameter describing the composition of particles. Organic particles consist of soft watery protoplasm that results in low refractive indices relative to water (1.02–1.08; Aas, 1996; Babin et al., 2003). Inorganic particles include various minerals or shell material produced by organisms, so they have higher refractive indices (1.15–1.20; Stramski et al., 2004; Zaneveld et al., 1974). The particulate backscattering ratio (*bbr*, the ratio of backscattering to total scattering by particles, b_{bp}/b_p) provides a proxy of bulk index of refraction of the assemblages and hence of composition; however, *bbr* also is affected by the PSD because small-sized particles have high backscattering efficiency (Boss et al., 2004; Twardowski et al., 2001). The *bbr* value indicates the dominance of organic ($bbr \sim 0.005$) versus inorganic ($bbr \sim 0.02$) composition of the suspended particles when the PSD is not very steep (Twardowski et al., 2001). When it is steep ($\xi > 4.4$), *bbr* is sensitive to size (e.g., Boss et al., 2007).

1.2. CRE Background

The CRE, at the border between Oregon and Washington in the USA, is affected by large tidal currents, strong winds, and seasonally varying river discharges, all of which influence plume dynamics and associated sediment transport (Elias et al., 2012). The mean tidal range in the CRE is 2.4 m with a neap to spring range from 2 to 4 m. Peak tidal velocities in the narrow entrance channel can reach up to 3 m/s at the mouth during ebbs. Monthly average flow varies from 9,000 m^3/s in May to 3,500 m^3/s in September, and annual mean flow is 7,300 m^3/s at Dalles (Bottom et al., 2005; MacCready et al., 2009). The largest monthly average flows are observed during May-June freshets, due to snowmelt in the eastern subbasin (Fain et al., 2001). Weaker winter freshets are fed primarily by coastal tributaries, while the smallest flows occur during late summer when precipitation and snowmelt runoff are minimal (Hudson et al., 2017). Suspended sediment in the CRE is primarily of fluvial origin, composed mostly of fine particles (silt and clay) and aggregates (Jay & Smith, 1990). SPM concentration is typically less than 100 g/m^3 throughout the CRE (Fain et al., 2001). The present sediment discharge is ~8 million tons per year (Spahn et al., 2009), and about 70% of the fine particles move through the estuary and into the ocean (Nowacki et al., 2012).

The CRE has a pronounced ETM due to particle trapping caused by convergent tidal shear fluxes, strong currents that resuspend material from the bed, and a robust internal circulation (Fain et al., 2001; Jay & Musiak, 1994). The strength and positioning of the ETM largely controls the distribution of the SPM. Because ETMs are typically found near or seaward of the upstream limits of salinity intrusions (Fain et al., 2001; Jay & Musiak, 1994), the magnitude and location of the ETM depends on the strength of the tides, river flow, and stratification (Geyer, 1993; Hudson et al., 2017; Jay & Smith, 1990). The CRE changes from a weakly to strongly stratified estuary within a spring-neap cycle (Jay & Smith, 1990). During neap tides, reduced vertical mixing and higher stratification result in increased salinity intrusion and upstream movement of the ETM. By contrast, high flow conditions during spring tides exhibit increased vertical mixing and lower stratification, with downstream movement of the ETM (Hudson et al., 2017; Jay & Smith, 1990).

2. Materials and Methods

A profiling instrument package was deployed from the *R/V Point Sur* to measure water temperature and salinity, OPs (γ, γ_{bb}, b_{bp}, and *bbr*), PSD, SPM, and Chl along transects inside the CRE. The instrument package carried a Sequoia Scientific LISST-100X Type B, a Machine Vision Floc Camera (MVFC), a WET Labs ac-9 absorbance and attenuation sensor with a 10-cm pathlength and a WET Labs ECO BB2FL, a WET Labs WETStar CDOM (Colored Dissolved Organic Matter) Fluorometer, an RBR CTD (conductivity, temperature, and depth sensors), a SeaBird-37 CTD, and two pressure-actuated Niskin bottles. Data were collected on 44 descending profiles at a number of stations along the estuary (Figure 2). Particle and optical properties were measured in vertical profiles with profiling speed of 0.5 m/s. Measurements were made during 1–5 June 2013, a period corresponding to relatively high discharge conditions. Daily averaged flow was 8,930 m^3/s at Beaver Army Terminal during the measuring period. The predicted tidal current data were downloaded from National Oceanic and Atmospheric Administration Tides and Currents website (https://tidesandcurrents.noaa.gov/currents13) at Sand Island Tower midchannel station (Figure 2).

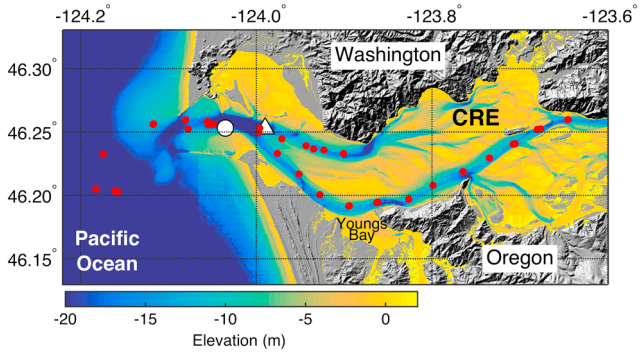

Figure 2. Map of the CRE with sampling stations (labeled by red dots and white dot). The anchor station is labeled by the white dot near the estuary entrance. Location of predicted tidal current is at Sand Island Tower (white triangle). Positions of sampling stations are plotted over a digital elevation model with 40-m horizontal resolution (Stevens et al., 2017), which was provided by U.S. Geological Survey. CRE = Columbia River Estuary.

2.1. PSD Measurements

The LISST-100X in situ particle sizing instrument operates on the principle of laser diffraction, and it has been used widely to estimate PSD and volume concentration $VC(D)$ (μL/L) in coastal waters (Agrawal & Pottsmith, 2000; Fugate & Friedrichs, 2002; Hill et al., 2011; Mikkelsen et al., 2005; Slade & Boss, 2015; Traykovski et al., 2004). The LISST uses near-forward laser light scattering to retrieve the in situ volume distribution of suspended particles. The LISST sampled continuously while in the water and was set to average 50 scans within 2 s, which were inverted to PSD using the manufacturer-provided software. LISST data were processed in MATLAB (The MathWorks, Inc., Natick, MA, http://www.mathworks.com) yielding an estimate of $VC(D)$. The spherical scattering property kernel matrix provided by Sequoia Scientific was used to convert the angular distribution of scattered light into a PSD. The size distributions were binned into 32 size bins ranging from 1.25 to 250 μm. Assuming all particles are spherical, $VC(D_i)$ in size bin i was converted to area size distribution $AC(D_i)$ (m^2/m^3; total cross-sectional area for a given size bin per volume; Neukermans et al., 2012).

The MVFC was programmed to take images continuously with an image interval of 5 s. The MVFC took gray-scale silhouette images of the suspended particles in the water column (Hill et al., 2011). Size analysis was performed with ImageJ (Image Processing and Analysis in Java, http://imagej.nih.gov/ij/). Images first were converted to binary images, using Triangle thresholding to determine the gray-scale value used to distinguish particles from the background (Zack et al., 1977). The Triangle threshold value is determined by normalizing the height and dynamic range of the pixel intensity histogram in an image (Tajima & Kato, 2011). In image analysis, an assumption of spherical particles was made to be consistent with LISST spherical shape particle model. The outputs were analyzed in MATLAB to detect particles with circularity values larger than 0.3 (a value 1.0 means a perfect circle). Elongated particles generally were diatom chains that were difficult to quantify precisely with the image analysis algorithms. Overall, approximately 16% of the particles in the images had circularities lower than 0.3, so area and volume concentrations were underestimated. This underestimation was deemed acceptable because the error associated with the assumption of sphericity during conversion of volume to area increases rapidly for circularities below 0.3. Nine pixels were chosen as the minimum number of pixels (3 × 3 pixels) to define a particle in an image, so the smallest particle resolved was approximately 36 μm in diameter (Mikkelsen et al., 2006). The largest particle observed in the images was approximately 540 μm in diameter in this study, but measurement range extended up to ~4 cm. Particle areas and equivalent spherical diameters were subsequently computed and binned into 37 logarithmically increasing bin sizes using the same class size widths as the LISST.

Because of MVFC and LISST have different data collection frequencies, each MVFC area distribution was merged with its corresponding LISST particle area distribution that was closest in time. The LISST and MVFC PSD overlapped across 12 bins (21 – 32) with median diameters from 34 to 212 μm. The overlap size bins 21 – 23 were selected as the *merge bins*. The proportion of area concentration from the LISST and from the MVFC in bin 21 was 75% and 25%, respectively. In size bins 22 and 23, the weight of LISST area concentration reduced to 50% and 25%, and the weight of MVFC area concentration raised to 50% and 75%, respectively. This weighted method produced smooth interpolation from LISST area concentration to MVFC area concentration. The size bins 1 – 5 were omitted to mitigate the influence of *rising tail* in the LISST size spectrum (Mikkelsen et al., 2005). The full merged particle area concentration distribution was formed with data from the LISST (bins 6 – 20), weighted data from the LISST and MVFC (bins 21 – 23), and data from the MVFC (bins 24 – 37). The merged area PSD extends from 2.85 to 540 μm. The $AC(D_i)$ was converted to $VC(D_i)$ based on the assumption of spherical geometry. Sauter mean diameter (D_s, in μm) was calculated using the merged PSD data, based on the total cross-sectional area and volumetric PSD,

$$D_s = \frac{1.5 \times \sum_{i=6}^{37} VC(D_i)}{\sum_{i=6}^{37} AC(D_i)}. \quad (3)$$

Sauter mean diameter is a descriptor of the size distribution that responds to the entire size distribution, including large particles. It is used here because of the focus on flocculation processes.

The LISST-100X instruments are challenged in stratified environments. In pycnoclines, the density differences can cause light scattering, called *schlieren*, that give rise to erroneous LISST PSDs. The buoyancy frequency (N, in s^{-1}) was used to define the likelihood of schlieren (Tao et al., 2017). The N was computed from RBR CTD data as (Thomson & Emery, 2014):

$$N = \left(-\frac{g}{\rho_0} \frac{\partial \rho}{\partial z} \right)^{0.5}, \tag{4}$$

where g (in m/s^2) is the gravitational acceleration, ρ_0 (in kg/m^3) is the average density during the downward profiling for each station, and $\frac{\partial \rho}{\partial z}$ is the vertical density gradient. An N larger than 0.05 s^{-1} was the threshold for schlieren effects in this study (Tao et al., 2017), which has been used to eliminate the inaccurate merged PSDs and values of D_s. In order to analyze D_s changes in the stratified layer, D_s was also obtained only from the MVFC. The D_s derived from MVFC were calculated using PSDs from 36 to 540 μm (size bins 21 to 37). To compare different properties, D_s and N were bin-averaged into 1-m depth bins from the surface to 10-m depth.

The exponent γ was estimated from each measured particulate attenuation spectrum $c_p(\lambda)$ (equation (2)). The attenuation coefficient and absorption coefficient were measured using a 10-cm pathlength WET Labs ac-9 (acceptance angle is 0.93°) spectral absorption and attenuation meter at nine wavelengths (λ = 412, 440, 488, 510, 532, 555, 650, 676, and 715 nm), at 6-Hz sampling rate (Twardowski et al., 1999). An ac-9 requires a pump to pull the water into the sensing zone of the instrument. A flow control switch (Sequoia Scientific FlowControl-Sub) allowed the ac-9 to collect either 0.2-μm-filtered or raw water samples. For each profile, the instrument package was lowered into the water, and the ac-9 collected filtered water samples. When the instrument reached 1.5 m below the surface, the flow control switch directed raw water into the intake of the ac-9. When the instrument reached a depth of 8 m, the switch was activated to direct the flow through the filter. The package continued to collect filtered water during the descent to the maximum depth of the profile and during the return to the surface. Upon reaching 1.5 m on the second downcast in each profile, the flow control switch changed to direct raw water into the instrument again. Another profile was collected in the same way, and after the second upcast the instrument package was recovered. Attenuation coefficients were corrected for temperature effect and the contribution by pure water (Pegau et al., 1997; Twardowski et al., 1999). The calibration-independent $c_p(\lambda)$ (in m^{-1}) was computed as follows (Boss et al., 2007):

$$c_p(\lambda) = c_{pg}(\lambda) - c_g(\lambda), \tag{5}$$

where $c_{pg}(\lambda)$ represents the total raw-water beam attenuation, which included water and dissolved plus particulate matter, and $c_g(\lambda)$ is the beam attenuation of water and the dissolved fraction smaller than 0.2 μm. Even though the $c_{pg}(\lambda)$ and $c_g(\lambda)$ were collected from downcast and upcast profiles, respectively, it is assumed that the optical properties of dissolved substances did not change between the downcasts and upcasts taken within less than 5 min of each other.

In this study, 40% of the $c_g(715)$ exhibited values of 0.05 m^{-1} or higher, significantly larger than expected (near 0), which were attributed to bubbles (these spectra were also variable within each depth bin). Those spectra were replaced with spectra reconstructed by regressing uncontaminated $c_g(\lambda)$ data with a CDOM fluorescence measured from WET Labs WETStar CDOM Fluorometer and with salinity measured from a SeaBird-37 CTD. The CDOM and salinity are linearly correlated with $c_g(\lambda)$ in estuarine systems (e.g., Wang & Xu, 2012), so the derived linear regressions were averaged to provide an estimated $c_g(\lambda)$.

The $c_p(\lambda)$ spectra from an ac-9 typically follow a power law function of wavelength. To eliminate attenuation coefficients affected by spikes associated with bubbles and rare larger particles, each spectrum was fitted to a power law, and the coefficients of determination (R^2) were calculated. In this study, 13% of the spectra had power law fits with values of R^2 less than 0.95, so they were excluded. This method was effective in removing anomalous values of γ.

The γ_{bb} estimated from $b_{bp}(\lambda)$ spectra is another indicator of particle size changes (Slade & Boss, 2015). The WET Labs ECO BB2FL sensor measures the volume-scattering function at a fixed angle in backward direction (124°), at two wavelengths of 532 and 650 nm ($\beta_{124}(\lambda)$, in $sr^{-1}\cdot m^{-1}$). The volume scattering function of particles ($\beta_{p124}(\lambda)$) was calculated from the difference between $\beta_{124}(\lambda)$ and $\beta_{w124}(\lambda)$. The scattering by water

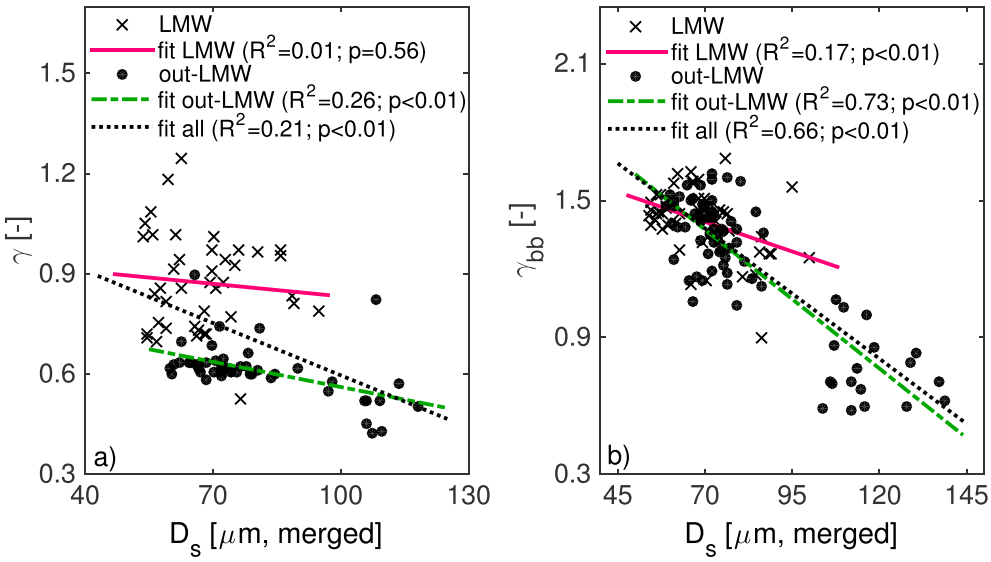

Figure 3. (a) Scatter plot of γ and D_s calculated from the merged data from a LISST-100X and a Machine Vision Floc Camera. (b) Scatter plot of γ_{bb} and D_s calculated from the merged data. The mark × indicates the data collected in low- to medium-salinity waters (LMW: $0.1 \le S \le 7$ PSU), and dot indicates the data collected out of low- to medium-salinity waters (out-LMW: $S < 0.1$ or $S > 7$ PSU). Black dotted line, red solid line, and green dash-dot line represent the least squares linear regression fits performed on all data, data collected in the LMW, and data collected out-LMW, respectively. The goodness of fit and statistical significance are expressed as coefficient of determination (R^2) and p value, respectively. LISST = Laser In-Situ Scattering and Transmissometry.

($\beta_{w124}(\lambda) \sim 10^{-5}$ sr^{-1}·m^{-1}) is negligible compared to scattering by particles ($\beta_{p124}(\lambda) \sim 10^{-2}$ sr^{-1}·m^{-1}) in turbid waters. The $\beta_{p124}(\lambda)$ was used to compute the particulate backscattering coefficient b_{bp} with units of m^{-1} through the formula $b_{bp}(\lambda) = 2\pi \times 1.14 \times \beta_{p124}(\lambda)$ (Boss & Pegau, 2001). Having obtained the two spectral values of $b_{bp}(\lambda)$ at 532 and 650 nm, γ_{bb} was calculated as

$$\gamma_{bb} = -\frac{log\left[b_{bp}(\lambda_1)/b_{bp}(\lambda_2)\right]}{log[\lambda_1/\lambda_2]}, \tag{6}$$

where $\lambda_1 = 532$ nm and $\lambda_2 = 650$ nm. The γ_{bb} was calculated using only two wavelengths, and γ_{bb} is sensitive to the computed wavelength range (McKee et al., 2009). Therefore, γ_{bb} only indicates the qualitative changes of PSD (Antoine et al., 2011). It is should be noted that γ_{bb} was previously found to be an adequate proxy of the proportion of fine particles versus large flocs (Many et al., 2016). Both γ and γ_{bb} are limited by the upper size limit of particles observed, each with their own size cutoff (Slade & Boss, 2015).

2.2. Particle Concentration Measurements

SPM (in g/m^3) was measured from water samples collected with the pressure-actuated Niskin bottles at 5- and 10-m depth and from water samples collected at the surface with a weighted, open-mouthed 1-L sample bottle deployed by hand from the deck of the ship. Water samples were filtered through preweighted 8-μm Millipore SCWP(cellulose acetate) filters on board the ship. These filters have effective pore sizes much smaller than 8 μm, and they are less prone to clogging than filters with smaller nominal pore sizes (Hill et al., 2013; Sheldon, 1972). The filters were rinsed with distilled water to remove accumulated salts and then dried and weighed in the lab. Tao et al. (2017) regressed these SPM measured from water samples against $b_{bp}(650)$ from ECO BB2FL, with correlation coefficient (R) of 0.76 and p value < 0.001 based on 92 samples, and their results indicate that the estimated $b_{bp}(650)$ is a robust proxy of the SPM concentration at the CRE.

Chlorophyll concentration was estimated using particulate absorption $a_p(\lambda)$, measured by the WET Labs ac-9. The calibration-independent $a_p(\lambda)$ (m^{-1}) was computed as

$$a_p(\lambda) = a_{pg}(\lambda) - a_g(\lambda), \tag{7}$$

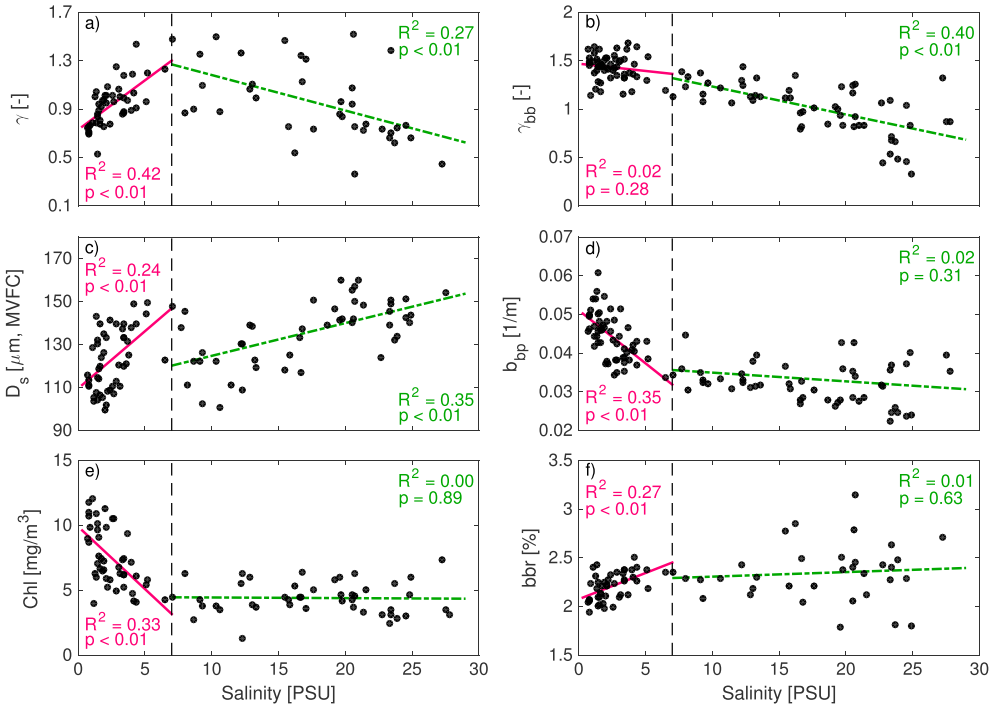

Figure 4. The variation of optical proxies along an estuarine salinity gradient with salinity ranging from 0.1 to 30 PSU. Measurements above 4-m depth only are included. Scatter plot of salinity versus (a) γ, (b) γ_{bb}, (c) D_s calculated only from a Machine Vision Floc Camera, (d) b_{bp}, (e) Chl, and (f) *bbr*. The black dashed line separates two zones (LMW and MHW) with salinities greater or less than 7 PSU. The red solid line and green dash-dot line represent the least squares regression line in each zone; the goodness of fit and statistical significance are expressed as R^2 and *p* value, respectively.

where $a_{pg}(\lambda)$ is total raw water absorption and $a_g(\lambda)$ is absorption of dissolved fraction smaller than 0.2 μm. The Chl (in mg/m^3) measurements were made using three red wavelengths following Boss et al. (2007) as

$$Chl = \frac{a_p(676) - \left(\frac{39}{65} \times a_p(650) + \frac{26}{65} \times a_p(715)\right)}{0.014}, \tag{8}$$

where the value of the chlorophyll-specific absorption $a^*(676)$ is equal to 0.014 m^2/(mg Chl). This absorption line height-based method is relatively accurate for determination of Chl concentration. The uncertainty is greatly reduced by subtracting the absorption measured on filtered samples from those measured on the raw water samples (Roesler & Barnard, 2013).

2.3. Optical Proxy for Particle Composition

The particulate backscattering ratio (*bbr*, b_{bp}/b_p) was calculated at a wavelength of 650 nm, using the b_{bp} derived from ECO BB2FL and particulate scattering (b_p) obtained from ac-9. The b_p was calculated as particulate attenuation minus absorption $\left(b_p(650) = c_p(650) - a_p(650)\right)$.

The median values of γ, γ_{bb}, $b_{bp}(650)$, Chl, and *bbr* were computed in every 1-m vertical bin from the surface to 10-m depth. As with optical data, a median-binning procedure minimized the contribution of spikes in the data associated with bubbles or rare large particles (Boss, Slade, Behrenfeld, et al., 2009; Whitmire et al., 2007).

3. Results

3.1. OPs for Particle Size

The γ derived from particulate attenuation spectrum with WET Labs ac-9 was inversely related to D_s calculated from the combined data of a LISST-100X and a MVFC (dotted line in Figure 3a), which is consistent with previous studies (Slade & Boss, 2015). A Model I linear regression fit between D_s and γ was significant at the 95% confidence level ($p < 0.01$); however, the R^2 was only equal to 0.21. This overall relationship between γ and D_s broke down at low- to medium-salinity waters (LMW: $0.1 < S < 7$ PSU, solid line in Figure 3a). The γ_{bb}, derived from particulate backscatter spectrum, was inversely and more strongly correlated with D_s ($R^2 = 0.66$,

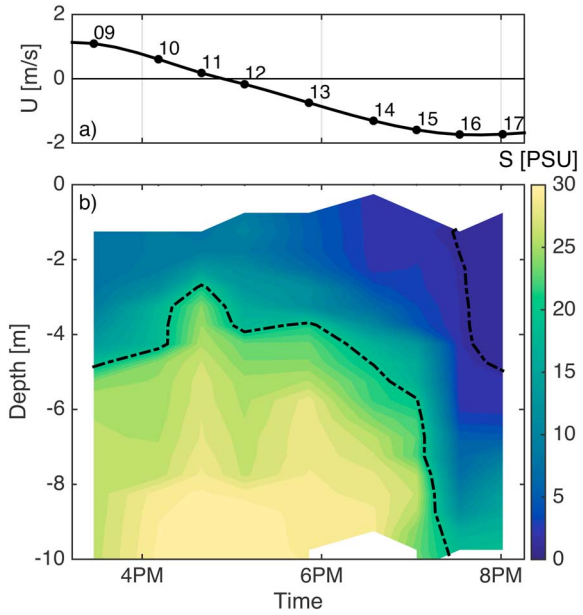

Figure 5. (a) Time series of predicted tidal current velocity at Sand Island Tower near the anchor station (labeled by white triangle in Figure 2, Cast 09-17) from flood to ebb tides. (b) Time series of vertical salinity profiles (*S*, in PSU) at the anchor station (labeled by white dot in Figure 2) shows the distribution of fresh river water and saline ocean water creating a pycnocline, which is the layer between two isohalines (black dash-dot lines: $S = 2$ PSU and $S = 20$ PSU).

$p < 0.01$; dotted line in Figure 3b). The correlation between γ_{bb} and D_s was weaker ($R^2 = 0.17$, $p < 0.01$) in the LMW (solid line in Figure 3b). Note that outliers, defined as γ_{bb} values that fell outside of the 95% prediction interval, were removed in the Model I linear regression analysis. Overall, the two OPs for particle size were correlated with D_s, but the correlation weakened or disappeared in the LMW.

3.2. OPs Along Salinity Gradient

In order to investigate the variation of particle and optical properties in the salinity transition region that was not affected by resuspension, the proxies collected from the top 4 m of the water column were used (Figure 4). The LMW and medium- to high-salinity waters (MHW) were separated by salinities of 7 PSU. Because LISST was affected by schlieren and fewer data were available in the stratified layer, D_s here were calculated only from the MVFC. The exponent γ increased as D_s increased from the LMW (Figures 4a and 4c). In contrast, γ_{bb} did not decrease with increasing salinity in the LMW (Figure 4b). In the MHW, D_s increased as γ and γ_{bb} decreased; b_{bp} and Chl values declined with increasing salinity in the LMW (Figures 4d and 4e). The increased *bbr* values likely indicated an increase in mineral content in the LMW, consistent with decreased Chl concentration (Figures 4e and 4f). The scattered *bbr* with relatively lower Chl concentration likely indicated the high variability in composition and PSD in the MHW.

3.3. Temporal Variability of OPs at Anchor Station

Time-series of measurements at the anchor station were made from flood to ebb tides (Figure 5a). Time series of vertical salinity profiles at the anchor station (Cast 09-17) showed the fresh water and saline ocean water converged at a density front (Figure 5b). A stratified water column with a pycnocline at ~5-m depth (labeled by the layer between two black dash-dot lines, $S = 2$ PSU and $S = 20$ PSU) existed seaward of the surface density front at the CRE mouth.

Time series of vertical profiles of PPs and OPs at the anchor station varied during the 4.5 hr of sampling (Figure 6). Higher D_s values (exceeding 95 μm) were observed in the saline water and lower D_s values (50–80 μm) were observed in the river water (Figure 6c). The D_s values declined upward away from the seabed in the bottom saline water. The exponent γ was larger in the river water than in the saline water, and the largest γ values were found in the pycnocline (Figure 6a). In the saline waters, larger D_s were found with smaller γ, suggesting that resuspension from the seabed and sinking from above brought larger particles near the bottom. The exponent of backscattering γ_{bb} and exponent of attenuation γ showed similar variation except in the pycnocline (Figures 6a and 6b). The γ_{bb} gradually decreased in the upper layer as the plume moved out.

The surface b_{bp} declined as the fresh plume moved out over the saline ocean water, and estimated Chl also decreased in the surface layer (Figures 6d and 6e). Also, the b_{bp} was larger near the density front. At the anchor station, the suspended particles were dominated by inorganic material as indicated by *bbr* values that exceeded 0.02. Lower *bbr* values indicated a more-organic particle population in the river water; *bbr* values were higher near the bottom (Figure 6f). The *bbr* values increased in the transition zone from the LMW. Particles with relatively higher *bbr*, consistent with a mineral-rich composition, were found in larger concentration in the vicinity of the density front.

4. Discussion

4.1. Spatial Patterns of Estuarine Particle Dynamics

Optical measurements provided a qualitative representation of spatial and temporal variations in particle size, concentration, and composition in the CRE that were broadly consistent with the established model (Figure 1). The optical measurements demonstrated that the river introduced a mixture of suspended particles to the CRE, including inorganic particles, medium-sized organic-rich particles, and large organic-rich particles. The density difference between riverine water and saline water produced a buoyant plume and a salinity intrusion near the river mouth. The surface b_{bp} measurements along the CRE indicated that the SPM concentration decreased as the river plume flowed out. The surface Chl concentration decreased as well. In

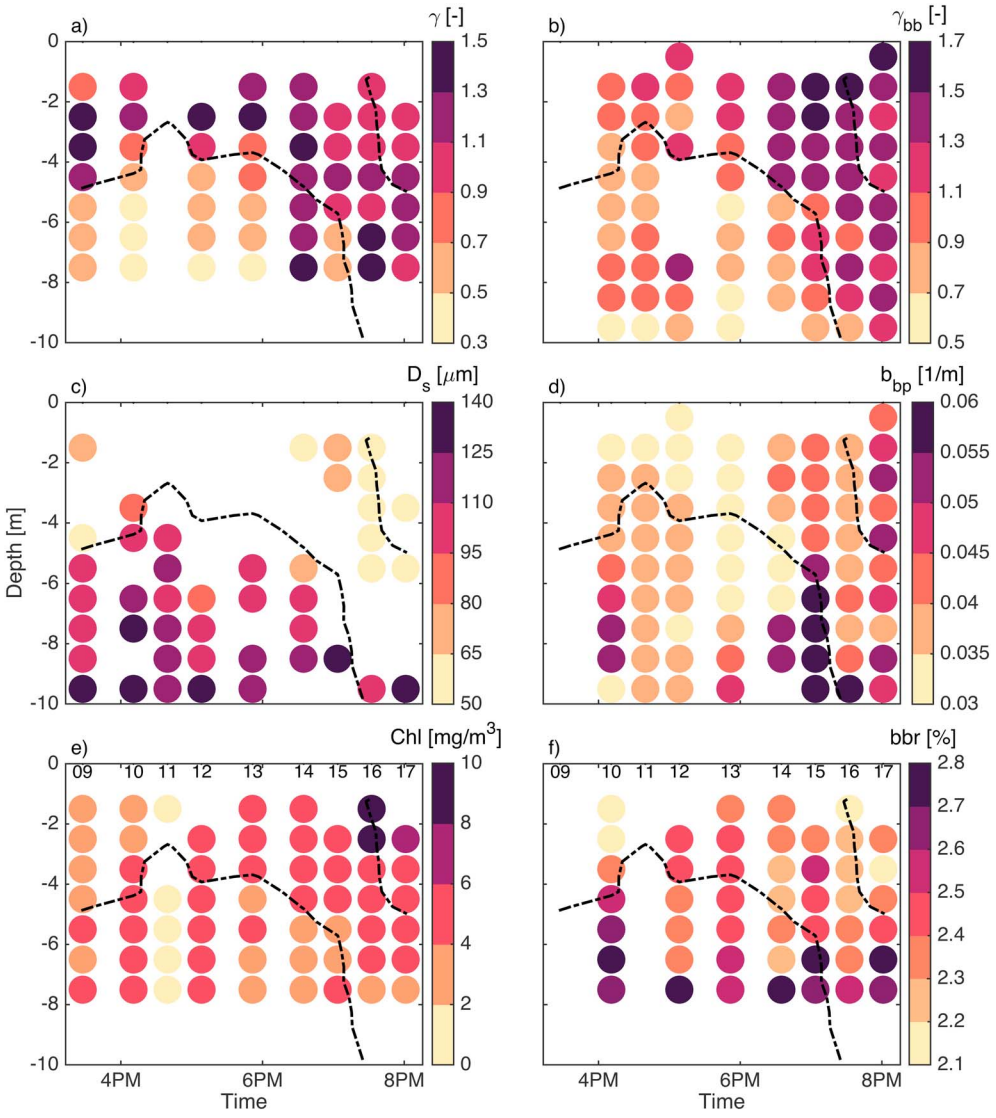

Figure 6. The temporal variability of optical proxies at the anchor station from flood to ebb tides. Time series of vertical profiles of (a) γ values estimated from particulate beam attenuation spectra that indicate particle size variation; (b) γ_{bb} values estimated from particulate backscattering that indicate particle size variation; (c) Sauter mean diameter D_s (in μm) as calculated from the combined data from a LISST-100X and a Machine Vision Floc Camera; (d) b_{bp} (in m^{-1}) values that indicate sediment concentration; (e) Chl (in mg/m^3) values estimated from particulate absorption; (f) *bbr* values that indicate particle composition variation. The layer between black dash-dot lines denote the pycnocline. In the D_s panel, the blank area in the pycnocline indicates the elimination of schlieren effects on LISST. LISST = Laser In-Situ Scattering and Transmissometry

general, the decreasing of SPM concentration in estuaries results from numerous physical and biological processes, such as gravitational sinking, physical mixing with water containing less particles and consumption of particulate organic matter (Burd & Jackson, 2009). Particle gravitational sinking is a primary mechanism behind removal of suspended particles from the water column in estuaries; b_{bp} and Chl declined significantly in the LMW, reflecting SPM concentration decrease most likely by particle sinking. The γ_{bb} declined in the upper layer as the plume moved out, suggesting that suspended particles were forming larger-sized particles along the flow (Figure 6). Observations demonstrated that particle concentration in the upper layer decreased because of formation and sinking of flocs. D_s was smaller in the upper river water (Figure 6b), and it increased with increasing salinity in the transition zone as flocculation continued (Figure 4c). In the LMW, some of newly formed large flocs sank to the seabed. The large flocs formed mostly by combining more organic-rich material

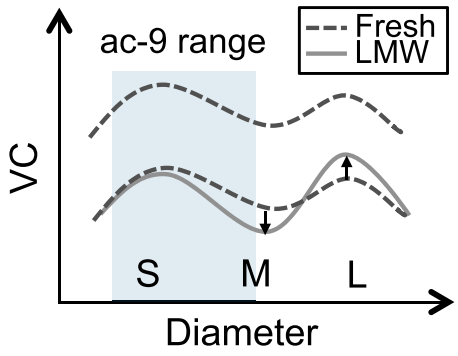

Figure 7. Schematic diagram illustrates proposed variation of merged volumetric PSDs in the LMW. The dashed curve and solid curve represent the PSD in the fresh water and LMW, respectively. The dashed curve moves down as particle concentration decreases from fresh water to LMW. Comparing PSDs in the fresh water (lower dashed curve) and LMW, flocculation transfers mass preferentially from medium-sized particles (M) to large-sized particles (L) that are out of the range of ac-9 (shaded area). The γ is a proxy of the proportion of small particles (S) versus M, and γ_{bb} is a proxy of the proportion of S versus M plus L. According to this conceptual model, flocculation transferring mass from M to L would increase γ, but the effect on γ_{bb} would be weaker. LMW = low- to medium-salinity waters; PSD = particle size distribution.

as *bbr* increased. In the MHW, the particle size D_s also increased in the plume as γ and γ_{bb} decreased, which was consistent with the conceptual model that particles grow continuously larger in the surface layer due to flocculation of river sediment with locally produced particles, and small flocs were transported seaward over the salinity intrusion (Figures 1 and 4).

The patterns of OPs reported here also indicated that larger tidal currents resuspended mineral-rich and larger particles from the seabed, which accumulated in the vicinity of the density front (Figure 1). Note that those trapped particles may have been aggregates that were compacted and toughened by multiple rounds of resuspension and deposition. The peak b_{bp} with higher *bbr* were observed near the bottom in the vicinity of the density front, and D_s was larger and decreased upward in the bottom layer (Figure 6). These observations may indicate sinking particles were resuspended by larger tidal currents and transported landward, resulting in the estuarine convergence of sediment flux and sediment trapping in the ETM (Geyer et al., 1997; Postma, 1967; Traykovski et al., 2004).

4.2. OPs for Particle Size in Salinity Transition

In the salinity transition region, the measurements only from the top 4 m of the water column were investigated because the particle and optical properties in the surface layer were less affected by resuspension. Therefore, the patterns of changes could be related more clearly to flocculation and deposition. Patterns of variation in OPs for particle size emerged in the transition zone from LMW that indicated complicated particle dynamics. Outside of the LMW, the exponent of the attenuation spectrum γ was inversely correlated with merged D_s (dash-dot line in Figure 3a), which is consistent with previous studies. However, the exponent γ increased in the LMW (Figure 4a), and γ was not correlated with merged D_s in the LMW (solid line in Figure 3a). The exponent γ derived from the ac-9 increased in the LMW, indicating the particle population dominating the ac-9 decreased in size. The measured D_s increased with increasing salinity in the LMW, suggesting that suspended particles were forming larger flocs (Figure 4c). The increase in the size was associated with particle sinking. The measured b_{bp} decreased with increasing salinity in the low-to-medium-salinity region, which indicated that particles deposited and SPM concentration decreased. The *bbr* increased from 0.02 to 0.025 in the transition zone, which indicates variability in particle composition, size distribution, or both. The *bbr* changes may have been caused by an increasing fraction of inorganic matter or by a steep particle size slope (Boss et al., 2004; Twardowski et al., 2001). The decreased Chl concentration in the surface water suggests that *bbr* increased due to loss of organic matter by sinking and deposition (Figures 4e and 4f). Previous studies have proposed an empirical power law relationship between *bbr* and Chl concentration for coastal waters (Huot et al., 2007; Sullivan et al., 2005). In general, previous studies observed increasing *bbr* with decreasing Chl concentration in coastal waters and indicated a lower percentage of organic particles (e.g., phytoplankton) with higher *bbr* suspended in the water column (Boss et al., 2004; Sullivan et al., 2005). As Chl concentration significantly decreased in the LMW, our observations were consistent with previously described behavior that *bbr* increased with an decrease in organic content, so the *bbr* changes in the LMW most likely was associated with composition changes. In the MHW, the scattered *bbr* with relatively lower Chl concentration indicated the high variability in composition and PSD, which was consistent with the conceptual model of mixing of riverine and estuarine particles.

One possible explanation for the unexpected increase in γ when particle size was increasing is the loss of medium-sized, inorganic silt and sand particles, which sink faster than large particles because they are denser, as seabed stress decreased. This simple explanation allows D_s to go up and γ to increase as well. Sauter diameter increases by removal of particles that are smaller than flocs, and γ increases because of loss of particles in the upper part of the size distribution that affects attenuation measured by the ac-9. The size range of particles that influence the spectral exponent γ has a limit (appropriate particle size range of 0.5 to 30 μm, Boss, Slade, Behrenfeld, et al., 2009) because the ac-9 has a relatively large acceptance angle, so large particles that scatter in the very near-forward direction are less efficiently detected. As denser, inorganic silt and sand particles are deposited, material remaining in suspension would have become more organic. This explanation is not supported by the observed increase in *bbr* from LMW, which indicates that the suspension likely became richer in mineral particles (Figure 4f).

Table 1
Summary of Particle Size Range and Key Limitations for Each Technology

Technology	Size range	Key limitations
γ (ac-9)	0.1–30 μm	Not sensitive to large particles; floc breakup in intake of instrument
γ_{bb}	unknown	Uncertainty in the LMW; sensitive to shape of absorption spectra
LISST-B	1.25–250 μm	Size distributions degraded by schlieren; particles larger than the upper size limit of the instrument
LISST-C	2.5–500 μm	Same as LISST-B
MVFC	36–540 μm (<4 cm)	Low sampling rate; does not resolve small particles

Note. LISST = Laser In-Situ Scattering and Transmissometry; LMW = low- to medium-salinity waters; MVFC = Machine Vision Floc Camera.

The trends in OPs are consistent with flocculation and deposition of organic particles in the river. At low-to-medium salinities, flocculation transferred mass preferentially from medium-sized particles to large-sized particles that were out of the range of the ac-9 (Figure 7). As flocs continued to form, some of the newly flocculated mass was deposited at the same time, resulting in decreases in b_{bp} and Chl. This process allowed both γ and D_s to increase due to flocculation. The *bbr* values rose because the large flocs preferentially incorporated more organic-rich material and then deposited to the seabed (Figures 4e and 4f). The particles remaining in suspension were more mineral-rich material with relatively higher *bbr*.

Although previous work suggested that γ_{bb} varied in a similar manner to γ, it did not increase and was weakly correlated with D_s in the LMW (Figures 3b, 4b, and 4c). Our results confirmed that γ_{bb} was negatively correlated with merged D_s ($R^2 = 0.66$, $p < 0.01$; dotted line in Figure 3b), but the relationship between γ_{bb} and D_s was weaker ($R^2 = 0.17$, $p < 0.01$) in the LMW (solid line in Figure 3b). Many et al. (2016) indicated that the γ_{bb} is an adequate proxy of the proportion of fine particles versus large flocs, so the variation of γ_{bb} may not be sensitive to changes in the relative concentration of medium-sized particles. We propose that γ reflects the changes of the proportion of small-sized particles versus medium-sized particles (Figure 7). Thus, transferring mass from medium-sized particles to large-sized particles affected γ and D_s, but the effect on γ_{bb} was weaker.

Changing absorption of red light by particles in the transition from fresh to saline water also may have affected the correlation between particle size and γ_{bb}. Estapa et al. (2012) observed that particles from coastal waters on the Louisiana continental shelf absorbed more red light per unit of mass than particles from the Atchafalaya River. If in the CRE there was stronger absorption of red light by particles in waters with higher salinities in the LMW, then the attenuation spectrum would have flattened and the backscatter spectrum would have steepened. The steeper backscatter spectrum would have weakened the dependence of γ_{bb} on particle size. Estapa et al. (2012) proposed that changes in dissolved and particulate iron were responsible for changes in particle absorption of red light. Dissolved iron concentration within the CRE decreases rapidly between salinities of 0 and 10 (Buck et al., 2007), likely because of dissolved organic matter flocculation and deposition (e.g., Boyle et al., 1977; Sholkovitz, 1976, 1978). It is possible, therefore, that particulate and dissolved iron dynamics affect the relationship between γ_{bb} and size, but this hypothesis requires more research.

Multiple optical measurements were used here to resolve variation of particle size, and each technology has limitations (Table 1). The parameters γ and γ_{bb} are potentially useful proxies for particle size in stratified estuarine environments where it is difficult to get accurate PSDs with conventional particle size analysis techniques. It is instructive to consider what interpretation of particle dynamics in the CRE would emerge by relying on a reduced set of OPs. If only OPs b_{bp}, *bbr*, and γ were used, the observations would indicate that the proportion of medium-sized particles dominating the ac-9 decreased by sinking and flocs combining more organic-rich material deposited in the LMW. In contrast, if only b_{bp}, *bbr*, and γ_{bb} were used, the observations would indicate that there was no significant change in the ratio between fine particles and larger flocs in the LMW, and particles combining more organic-rich material were removed from suspension by deposition. Both interpretations miss the formation of large flocs observed by the camera in the LMW and thus underrepresent the role of flocculation in estuarine particle dynamics.

Our results demonstrated that measurements of optical backscatter in stratified waters are useful for inferring changes in particle size and concentration. Overall, γ_{bb} gradually declined along salinity gradient and D_s increased, except D_s jumped at $S = 7$ PSU (Figures 4b and 4c). In addition, the exponent γ_{bb} is a better proxy than γ for particle size (Figure 3), which agreed with Slade and Boss (2015). The most likely reason is that D_s is more sensitive to changes in large-sized particles. The ac-9 detects particle less than 30 um and the effect of larger particles on the attenuation spectrum is masked, so γ may not be correlated as well with D_s as γ_{bb}. b_{bp} also was recommended as a proxy for SPM in stratified waters (Tao et al., 2017).

4.3. Future Work

Estuaries are dynamic and complex environments where flocculation and deflocculation processes and changes in particulate composition are active in the transition from LMW. In general, OPs are useful for inferring particle distribution and dynamics in estuaries. However, the relationship between γ and D_s in the transition zone did not match with previous studies. Future work should examine whether flocculation removes sediment from the upper end of ac-9 size range. Also, more research is required to investigate whether changes in mass-specific absorption of red light by particles in the LMW changes the sensitivity of γ_{bb} to particle size.

5. Summary and Conclusions

This study explored the spatial and temporal variability of suspended particles and their properties using OPs within the CRE. Results demonstrated a classical estuarine sediment pattern in the CRE, suggesting that OPs are useful for studying estuarine sediment dynamics. Flocculation and sinking of suspended matter were inferred in the CRE at the density interface, while sediment resuspension and accumulation were found in the ETM zone. In addition, the variation of OPs in the transition from LMW suggested that particle flocculation transferred mass preferentially from medium-sized particles to large-sized particles. Large flocs preferentially incorporated more organic-rich material and some of the newly formed flocs deposited to the seabed. Likely due to the complex variation of particle size and composition, the γ and γ_{bb} were not correlated well with D_s in the LMW. Overall, the exponent γ_{bb} is a better proxy for particle size in stratified estuarine environments. Further research is needed to test our hypothetical model of the evolution of the size distribution and influence of absorption on OPs of particle size in the transition from fresh to saline water.

Acknowledgments
We thank Andrew G. Stevens from U.S. Geological Survey for kindly providing elevation data. This research was supported by the Office of Naval Research, grants N00014-13-1-0148 and N00014-15-1-2106 (PSH) and N00014-13-1-0146 (ESB), and aided by the able crew of the *R/V Point Sur*. The data are available at https://figshare.com/s/90f41b0371533e93d72d.

References

Aas, E. (1996). Refractive index of phytoplankton derived from its metabolite composition. *Journal of Plankton Research*, *18*(12), 2223–2249.
Agrawal, Y., & Pottsmith, H. (2000). Instruments for particle size and settling velocity observations in sediment transport. *Marine Geology*, *168*(1), 89–114.
Agrawal, Y., & Traykovski, P. (2001). Particles in the bottom boundary layer: Concentration and size dynamics through events. *Journal of Geophysical Research*, *106*(C5), 9533–9542.
Antoine, D., Siegel, D. A., Kostadinov, T., Maritorena, S., Nelson, N. B., Gentili, B., et al. (2011). Variability in optical particle backscattering in contrasting bio-optical oceanic regimes. *Limnology and Oceanography*, *56*(3), 955–973.
Babin, M., Morel, A., Fournier-Sicre, V., Fell, F., & Stramski, D. (2003). Light scattering properties of marine particles in coastal and open ocean waters as related to the particle mass concentration. *Limnology and Oceanography*, *48*(2), 843–859.
Bale, A., & Morris, A. (1987). In situ measurement of particle size in estuarine waters. *Estuarine, Coastal and Shelf Science*, *24*(2), 253–263.
Boss, E. S., Collier, R., Pegau, W., Larson, G., & Fennel, K. (2007). Measurements of spectral optical properties and their relation to biogeochemical variables and processes in Crater Lake, Crater Lake National Park, OR. *Long-term Limnological Research and Monitoring at Crater Lake, Oregon*, *574*, 149–159.
Boss, E., & Pegau, W. S. (2001). Relationship of light scattering at an angle in the backward direction to the backscattering coefficient. *Applied Optics*, *40*(30), 5503–5507.
Boss, E., Pegau, W. S., Gardner, W. D., Zaneveld, J. R. V., Barnard, A. H., Twardowski, M. S., et al. (2001). Spectral particulate attenuation and particle size distribution in the bottom boundary layer of a continental shelf. *Journal of Geophysical Research*, *106*(C5), 9509–9516.
Boss, E., Pegau, W., Lee, M., Twardowski, M., Shybanov, E., Korotaev, G., & Baratange, F. (2004). Particulate backscattering ratio at LEO 15 and its use to study particle composition and distribution. *Journal of Geophysical Research*, *109*, C01014. https://doi.org/10.1029/2002JC001514
Boss, E., Picheral, M., Leeuw, T., Chase, A., Karsenti, E., Gorsky, G., et al. (2013). The characteristics of particulate absorption, scattering and attenuation coefficients in the surface ocean; Contribution of the Tara Oceans expedition. *Methods in Oceanography*, *7*, 52–62.
Boss, E., Slade, W. H., Behrenfeld, M., & Dall'Olmo, G. (2009). Acceptance angle effects on the beam attenuation in the ocean. *Optics Express*, *17*(3), 1535–1550.
Boss, E., Slade, W., & Hill, P. (2009). Effect of particulate aggregation in aquatic environments on the beam attenuation and its utility as a proxy for particulate mass. *Optics Express*, *17*(11), 9408–9420.
Boss, E., Taylor, L., Gilbert, S., Gundersen, K., Hawley, N., Janzen, C., et al. (2009). Comparison of inherent optical properties as a surrogate for particulate matter concentration in coastal waters. *Limnology and Oceanography: Methods*, *7*(11), 803–810.
Boss, E., Twardowski, M. S., & Herring, S. (2001). Shape of the particulate beam attenuation spectrum and its inversion to obtain the shape of the particulate size distribution. *Applied Optics*, *40*(27), 4885–4893.
Bottom, D. L., Simenstad, C. A., Burke, J., Baptista, A. M., Jay, D. A., Jone, K. K., et al. (2005). Salmon at river's end: The role of the estuary in the decline and recovery of Columbia River salmon (NOAA Tech. Memo. NMFS-NWFSC-68). Columbia: U.S. Department of Commerce.

Boyle, E., Edmond, J., & Sholkovitz, E. (1977). The mechanism of iron removal in estuaries. *Geochimica et Cosmochimica Acta*, *41*(9), 1313–1324.
Braithwaite, K., Bowers, D., Smith, W. N., Graham, G., Agrawal, Y., & Mikkelsen, O. (2010). Observations of particle density and scattering in the Tamar Estuary. *Marine Geology*, *277*(1), 1–10.
Buck, K. N., Lohan, M. C., Berger, C. J., & Bruland, K. W. (2007). Dissolved iron speciation in two distinct river plumes and an estuary: Implications for riverine iron supply. *Limnology and Oceanography*, *52*(2), 843–855.
Burd, A. B., & Jackson, G. A. (2009). Particle aggregation. *Annual Review of Marine Science*, *1*, 65–90.
Creed, E. L., Pence, A. M., & Rankin, K. L. (2001). Inter-comparison of turbidity and sediment concentration measurements from an ADP, an OBS-3, and a LISST. *OCEANS, 2001, MTS/IEEE Conference and Exhibition* (Vol. 3, pp. 1750–1754). Escondito, CA.
Crump, B. C., Fine, L. M., Fortunato, C. S., Herfort, L., Needoba, J. A., Murdock, S., & Prahl, F. G. (2017). Quantity and quality of particulate organic matter controls bacterial production in the Columbia River estuary. *Limnology and Oceanography*, *62*(6), 2713–2731.
D'Sa, E. J., Miller, R. L., & McKee, B. A. (2007). Suspended particulate matter dynamics in coastal waters from ocean color: Application to the northern gulf of Mexico. *Geophysical Research Letters*, *34*, L23611. https://doi.org/10.1029/2007GL031192
Downing, J. (2006). Twenty-five years with OBS sensors: The good, the bad, and the ugly. *Continental Shelf Research*, *26*(17-18), 2299–2318.
Effler, S. W., Peng, F., O'Donnell, D. M., & Strait, C. (2013). The backscattering coefficient and its components in the great lakes: A review and synthesis. *Journal of Great Lakes Research*, *39*, 108–122.
Eisma, D., Bale, A., Dearnaley, M., Fennessy, M., Van Leussen, W., Maldiney, M.-A., et al. (1996). Intercomparison of in situ suspended matter (floc) size measurements. *Journal of Sea Research*, *36*(1-2), 3–14.
Eisma, D., Bernard, P., Cadee, G., Ittekkot, V., Kalf, J., Laane, R., et al. (1991). Suspended-matter particle size in some West-European estuaries; Part I: Particle-size distribution. *Netherlands Journal of Sea Research*, *28*(3), 193–214.
Eisma, D., Boon, J., Groenewegen, R., Ittekkot, V., Kalf, J., & Mook, W. (1983). Observations on macro-aggregates, particle size and organic composition of suspended matter in the Ems estuary. *Mitteilungen aus dem Geologisch-Palaontologischen Institut der Universitat Hamburg*, *55*, 295–314.
Elias, E. P., Gelfenbaum, G., & Van der Westhuysen, A. J. (2012). Validation of a coupled wave-flow model in a high-energy setting: The mouth of the Columbia River. *Journal of Geophysical Research*, *117*, 21. https://doi.org/10.1029/2012JC008105
Ellis, K., Bowers, D., & Jones, S. (2004). A study of the temporal variability in particle size in a high-energy regime. *Estuarine Coastal and Shelf Science*, *61*(2), 311–315.
Estapa, M. L., Boss, E., Mayer, L. M., & Roesler, C. S. (2012). Role of iron and organic carbon in mass-specific light absorption by particulate matter from Louisiana coastal waters. *Limnology and Oceanography*, *57*(1), 97–112.
Fain, A. M., Jay, D. A., Wilson, D. J., Orton, P. M., & Baptista, A. M. (2001). Seasonal and tidal monthly patterns of particulate matter dynamics in the Columbia River estuary. *Estuaries*, *24*(5), 770–786.
Fugate, D. C., & Friedrichs, C. T. (2002). Determining concentration and fall velocity of estuarine particle populations using ADV, OBS and LISST. *Continental Shelf Research*, *22*(11), 1867–1886.
Gartner, J. W., Cheng, R. T., Wang, P.-F., & Richter, K. (2001). Laboratory and field evaluations of the LISST-100 instrument for suspended particle size determinations. *Marine Geology*, *175*(1-4), 199–219.
Geyer, W. R. (1993). The importance of suppression of turbulence by stratification on the estuarine turbidity maximum. *Estuaries*, *16*(1), 113–125.
Geyer, W., Signell, R., & Kineke, G. (1997). Lateral trapping of sediment in partially mixed estuary. In *Proceedings of the 8th International Biennial Conference on Physics of Estuaries and Coastal Seas* (pp. 115–124). Netherlands.
Guo, C., He, Q., Guo, L., & Winterwerp, J. C. (2017). A study of in-situ sediment flocculation in the turbidity maxima of the Yangtze Estuary. *Estuarine, Coastal and Shelf Science*, *191*, 1–9.
Hill, P., Boss, E., Newgard, J., Law, B., & Milligan, T. (2011). Observations of the sensitivity of beam attenuation to particle size in a coastal bottom boundary layer. *Journal of Geophysical Research*, *116*, C02023. https://doi.org/10.1029/2010JC006539
Hill, P. S., Fox, J. M., Crockett, J. S., Curran, K. J., Friedrichs, C. T., Geyer, W. R., et al. (2007). Sediment delivery to the seabed on continental margins. In *Continental margin sedimentation: From sediment transport to sequence stratigraphy, International Association of Sedimentologists* (Vol. 37, pp. 49–99). Oxford, UK: Blackwell.
Hill, P. S., Milligan, T. G., & Geyer, W. R. (2000). Controls on effective settling velocity of suspended sediment in the Eel River flood plume. *Continental Shelf Research*, *20*(16), 2095–2111.
Hill, P., Newgard, J., Law, B., & Milligan, T. (2013). Flocculation on a muddy intertidal flat in Willapa Bay, Washington, Part II: Observations of suspended particle size in a secondary channel and adjacent flat. *Continental Shelf Research*, *60*, S145–S156.
Huang, J., Chen, X., Jiang, T., Yang, F., Chen, L., & Yan, L. (2016). Variability of particle size distribution with respect to inherent optical properties in Poyang Lake, China. *Applied optics*, *55*(22), 5821–5829.
Hudson, A. S., Talke, S. A., & Jay, D. A. (2017). Using satellite observations to characterize the response of estuarine turbidity maxima to external forcing. *Estuaries and Coasts*, *40*(2), 343–358.
Hulst, H. C., & van de Hulst, H. C. (1957). *Light scattering by small particles*. New York: Courier Corporation.
Huot, Y., Morel, A., Twardowski, M., Stramski, D., & Reynolds, R. (2007). Particle optical backscattering along a chlorophyll gradient in the upper layer of the eastern South Pacific Ocean. *Biogeosciences Discussions*, *4*(6), 4571–4604.
Jay, D. A., & Musiak, J. D. (1994). Particle trapping in estuarine tidal flows. *Journal of Geophysical Research*, *99*(C10), 20,445–20,461.
Jay, D. A., & Smith, J. D. (1990). Circulation, density distribution and neap-spring transitions in the Columbia River estuary. *Progress in Oceanography*, *25*(1), 81–112.
Jones, D., & Wills, M. (1956). The attenuation of light in sea and estuarine waters in relation to the concentration of suspended solid matter. *Journal of the Marine Biological Association of the United Kingdom*, *35*(02), 431–444.
Jouon, A., Ouillon, S., Douillet, P., Lefebvre, J. P., Fernandez, J. M., Mari, X., & Froidefond, J.-M. (2008). Spatio-temporal variability in suspended particulate matter concentration and the role of aggregation on size distribution in a coral reef lagoon. *Marine Geology*, *256*(1), 36–48.
Kranck, K., & Milligan, T. (1992). Characteristics of suspended particles at an 11-hour anchor station in San Francisco Bay, California. *Journal of Geophysical Research*, *97*(C7), 11,373–11,382.
MacCready, P. (1999). Estuarine adjustment to changes in river flow and tidal mixing. *Journal of Physical Oceanography*, *29*(4), 708–726.
MacCready, P., Banas, N. S., Hickey, B. M., Dever, E. P., & Liu, Y. (2009). A model study of tide-and wind-induced mixing in the Columbia River Estuary and plume. *Continental Shelf Research*, *29*(1), 278–291.
Many, G., Bourrin, F., de Madron, X. D., Pairaud, I., Gangloff, A., Doxaran, D., & others. (2016). Particle assemblage characterization in the Rhone River ROFI. *Journal of Marine Systems*, *157*, 39–51.
McGuirk Flynn, A. (2008). Organic matter and nutrient cycling in a coastal plain estuary: Carbon, nitrogen, and phosphorus distributions, budgets, and fluxes. *Journal of Coastal Research*, *55*, 76–94.

McKee, D., Chami, M., Brown, I., Calzado, V. S., Doxaran, D., & Cunningham, A. (2009). Role of measurement uncertainties in observed variability in the spectral backscattering ratio: A case study in mineral-rich coastal waters. *Applied Optics*, *48*(24), 4663–4675.
McKee, D., & Cunningham, A. (2006). Identification and characterisation of two optical water types in the Irish Sea from in situ inherent optical properties and seawater constituents, estuarine. *Coastal and Shelf Science*, *68*(1), 305–316.
Mikkelsen, O. A., Hill, P. S., & Milligan, T. G. (2006). Single-grain, microfloc and macrofloc volume variations observed with a LISST-100 and a digital floc camera. *Journal of Sea Research*, *55*(2), 87–102.
Mikkelsen, O. A., Hill, P. S., Milligan, T. G., & Chant, R. J. (2005). In situ particle size distributions and volume concentrations from a LISST-100 laser particle sizer and a digital floc camera. *Continental Shelf Research*, *25*(16), 1959–1978.
Mikkelsen, O. A., Milligan, T. G., Hill, P. S., Chant, R. J., Jago, C. F., Jones, S. E., et al. (2008). The influence of schlieren on in situ optical measurements used for particle characterization. *Limnology and Oceanography: Methods*, *6*(3), 133–143.
Milligan, T. G., Hill, P., & Law, B. (2007). Flocculation and the loss of sediment from the Po River plume. *Continental Shelf Research*, *27*(3), 309–321.
Milligan, T., Kineke, G., Blake, A., Alexander, C., & Hill, P. (2001). Flocculation and sedimentation in the ACE basin, South Carolin. *Estuaries and Coasts*, *24*(5), 734–744.
Morel, A. (1973). Diffusion de la lumiere par les eaux de mer. résultats expérimentaux et approche théorique. *Optics of the Sea*, *61*, 3–1.
Neukermans, G., Loisel, H., Mériaux, X., Astoreca, R., & McKee, D. (2012). In situ variability of mass-specific beam attenuation and backscattering of marine particles with respect to particle size, density, and composition. *Limnology and Oceanography*, *57*(1), 124–144.
Nowacki, D. J., Horner-Devine, A. R., Nash, J. D., & Jay, D. A. (2012). Rapid sediment removal from the Columbia River plume near field. *Continental Shelf Research*, *35*, 16–28.
Pegau, W. S., Gray, D., & Zaneveld, J. R. V. (1997). Absorption and attenuation of visible and near-infrared light in water: Dependence on temperature and salinity. *Applied Optics*, *36*(24), 6035–6046.
Peng, F., & Effler, S. W. (2007). Suspended minerogenic particles in a reservoir: Light-scattering features from individual particle analysis. *Limnology and Oceanography*, *52*(1), 204–216.
Postma, H. (1967). Sediment transport and sedimentation in the estuarine environment. *American Association of Advanced Sciences*, *83*, 158–179.
Pritchard, D. (1967). *What is an estuary: A physical viewpoint* (pp. 3–5). Washington, DC: Estuaries. American Association for the Advancement of Science.
Reynolds, R. A., Stramski, D., & Neukermans, G. (2016). Optical backscattering by particles in arctic seawater and relationships to particle mass concentration, size distribution, and bulk composition. *Limnology and Oceanography*, *61*(5), 1869–1890.
Reynolds, R., Stramski, D., Wright, V., & Woźniak, S. (2010). Measurements and characterization of particle size distributions in coastal waters. *Journal of Geophysical Research*, *115*, C08024. https://doi.org/10.1029/2009JC005930
Roesler, C. S., & Barnard, A. H. (2013). Optical proxy for phytoplankton biomass in the absence of photophysiology: Rethinking the absorption line height. *Methods in Oceanography*, *7*, 79–94.
Sahin, C., Verney, R., Sheremet, A., & Voulgaris, G. (2017). Acoustic backscatter by suspended cohesive sediments: Field observations, Seine Estuary, France. *Continental Shelf Research*, *134*, 39–51.
Sheldon, R. (1972). Size separation of marine seston by membrane and glass-fiber filters. *Limnology and Oceanography*, *17*(3), 494–498.
Sholkovitz, E. (1976). Flocculation of dissolved organic and inorganic matter during the mixing of river water and seawater. *Geochimica et Cosmochimica Acta*, *40*(7), 831–845.
Sholkovitz, E. R. (1978). The flocculation of dissolved Fe, Mn, Al, Cu, NI, Co and Cd during estuarine mixing. *Earth and Planetary Science Letters*, *41*(1), 77–86.
Slade, W. H., & Boss, E. (2015). Spectral attenuation and backscattering as indicators of average particle size. *Applied Optics*, *54*(24), 7264–7277.
Small, L. F., & Prahl, F. G. (2004). A particle conveyor belt process in the Columbia River estuary: Evidence from chlorophyll a and particulate organic carbon. *Estuaries*, *27*(6), 999–1013.
Snyder, W. A., Arnone, R. A., Davis, C. O., Goode, W., Gould, R. W., Ladner, S., et al. (2008). Optical scattering and backscattering by organic and inorganic particulates in US coastal waters. *Applied Optics*, *47*(5), 666–677.
Spahn, E. Y., Horner-Devine, A. R., Nash, J. D., Jay, D. A., & Kilcher, L. (2009). Particle resuspension in the Columbia river plume near field. *Journal of Geophysical Research*, *114*, C00B14. https://doi.org/10.1029/2008JC004986
Spinrad, R. W., Zaneveld, J. R. V., & Kitchen, J. C. (1983). A study of the optical characteristics of the suspended particles in the benthic nepheloid layer of the Scotian Rise. *Journal of Geophysical Research*, *88*(C12), 7641–7645.
Stevens, A., Gelfenbaum, G., MacMahan, J., Reniers, A., Elias, E., Sherwood, C., & Carlson, E. (2017). *Oceanographic measurements and hydrodynamic modeling of the mouth of the Columbia River, Oregon and Washington, 2013*. U.S. Geological Survey data release. https://doi.org/10.5066/F7NG4NS1
Stramska, M., Stramski, D., Hapter, R., Kaczmarek, S., & Stoń, J. (2003). Bio-optical relationships and ocean color algorithms for the north polar region of the Atlantic. *Journal of Geophysical Research*, *108*, 3143. https://doi.org/10.1029/2001JC001195
Stramski, D., Boss, E., Bogucki, D., & Voss, K. J. (2004). The role of seawater constituents in light backscattering in the ocean. *Progress in Oceanography*, *61*(1), 27–56.
Stramski, D., & Kiefer, D. A. (1991). Light scattering by microorganisms in the open ocean. *Progress in Oceanography*, *28*(4), 343–383.
Sullivan, J. M., Twardowski, M. S., Donaghay, P. L., & Freeman, S. A. (2005). Use of optical scattering to discriminate particle types in coastal waters. *Applied Optics*, *44*(9), 1667–1680.
Tajima, R., & Kato, Y. (2011). Comparison of threshold algorithms for automatic image processing of rice roots using freeware ImageJ. *Field Crops Research*, *121*(3), 460–463.
Tao, J., Hill, P. S., Boss, E. S., & Milligan, T. G. (2017). Evaluation of optical proxies for suspended particulate mass in stratified waters. *Journal of Atmospheric and Oceanic Technology*, *34*(10), 2203–2212.
Thomson, R. E., & Emery, W. J. (2014). *Data analysis methods in physical oceanography*. Waltham, Massachusetts; Oxford, England; Amsterdam, Netherlands: Elsevier.
Traykovski, P., Geyer, R., & Sommerfield, C. (2004). Rapid sediment deposition and fine-scale strata formation in the Hudson estuary. *Journal of Geophysical Research*, *109*, F02004. https://doi.org/10.1029/2006JC003811
Twardowski, M. S., Boss, E., Macdonald, J. B., Pegau, W. S., Barnard, A. H., & Zaneveld, J. R. V. (2001). A model for estimating bulk refractive index from the optical backscattering ratio and the implications for understanding particle composition in case I and case II waters. *Journal of Geophysical Research*, *106*(C7), 14,129–14,142.
Twardowski, M. S., Sullivan, J. M., Donaghay, P. L., & Zaneveld, J. R. V. (1999). Microscale quantification of the absorption by dissolved and particulate material in coastal waters with an ac-9. *Journal of Atmospheric and Oceanic Technology*, *16*(6), 691–707.

Volz, F. (1954). Die optik und meteorologie der atmosphärischen trübung; mit 10 tabellen. Ber. Dtsch. Wetterdienstes.
Wang, F., & Xu, Y. J. (2012). Remote sensing to predict estuarine water salinity. In *Environmental remote sensing and systems analysis* (pp. 85–108). Boca Raton, FL: Taylor & Francis Group/CRC Press.
Whitmire, A. L., Boss, E., Cowles, T. J., & Pegau, W. S. (2007). Spectral variability of the particulate backscattering ratio. *Optics express*, *15*(11), 7019–7031.
Wolanski, E. (2007). *Estuarine ecohydrology*. Amsterdam, Netherlands: Elsevier.
Wolanski, E., & Gibbs, R. J. (1995). Flocculation of suspended sediment in the Fly River estuary, Papua New Guinea. *Journal of Coastal Research*, *11*, 754–762.
Woźniak, S. B., Stramski, D., Stramska, M., Reynolds, R. A., Wright, V. M., Miksic, E. Y., et al. (2010). Optical variability of seawater in relation to particle concentration, composition, and size distribution in the nearshore marine environment at imperial beach, California. *Journal of Geophysical Research*, *115*, C08027. https://doi.org/10.1029/2009jc005554
Xi, H., Larouche, P., Tang, S., & Michel, C. (2014). Characterization and variability of particle size distributions in Hudson Bay, Canada. *Journal of Geophysical Research: Oceans*, *119*, 3392–3406. https://doi.org/10.1002/2013JC009542
Zack, G., Rogers, W., & Latt, S. (1977). Automatic measurement of sister chromatid exchange frequency. *Journal of Histochemistry & Cytochemistry*, *25*(7), 741–753.
Zaneveld, J. R. V., Roach, D. M., & Pak, H. (1974). The determination of the index of refraction distribution of oceanic particulates. *Journal of Geophysical Research*, *79*(27), 4091–4095.